Prediction of Acute Graft Rejection after Liver Transplantation by Single Cell RNA Sequencing Analysis Using Peripheral Blood Mononuclear Cell

Kim, Deok-Gie

Department of Medicine
Graduate School
Yonsei University

Prediction of Acute Graft Rejection after Liver Transplantation by Single Cell RNA Sequencing Analysis Using Peripheral Blood Mononuclear Cell

Advisor Joo, Dong Jin

A Dissertation Submitted
to the Department of Medicine
and the Committee on Graduate School
of Yonsei University in Partial Fulfillment of the
Requirements for the Degree of
Doctor of Philosophy in Medical Science

Kim, Deok-Gie
June 2025

Prediction of Acute Graft Rejection after Liver Transplantation by Single Cell RNA Sequencing Analysis Using Peripheral Blood Mononuclear Cell

This Certifies that the Dissertation
of Kim, Deok-Gie is Approved

Committee Chair	Kim, Seung Up
Committee Member	Joo, Dong Jin
Committee Member	Hwang, Byungjin
Committee Member	Kwon, Ho-Keun
Committee Member	Kim, Jong Man

Department of Medicine
Graduate School
Yonsei University
June 2025

ACKNOWLEDGEMENTS

I extend my sincere gratitude to my supervisor, Dr. Joo, Dong Jin, for his invaluable guidance and steadfast support throughout this research. I am also deeply thankful to my former supervisor, Dr. Kim, Myoung Soo, whose mentorship has greatly shaped my academic path.

I would like to express my appreciation to the members of my thesis committee—Dr. Kim, Seung Up, Dr. Hwang, Byungjin, Dr. Kwon, Ho-Keun, and Dr. Kim, Jong Man—for their thoughtful feedback and constructive suggestions that strengthened this dissertation.

My heartfelt thanks to Dr. Lee, Su-Hyeon and Cho, Yuri for their dedicated assistance. I am also grateful to and The Research Institute for Transplantation in Yonsei University for providing essential resources.

Finally, I wish to express deep appreciation to my family. To my parents, for their love and sacrifices; to my son and daughters, whose presence gives me purpose; and to my wife, my partner and closest supporter—thank you for your unwavering love.

Kim, Deok-Gie

TABLE OF CONTENTS

LIST OF FIGURES

ABSTRACT

Prediction of Acute Graft Rejection after Liver Transplantation by Single Cell RNA Sequencing Analysis Using Peripheral Blood Mononuclear Cell

Liver transplantation remains a definitive therapy for end-stage liver disease; however, acute allograft rejection occurs in 15–30% of recipients. Early prediction is limited by the incomplete characterization of subclinical immune alterations, and diagnosis still depends on invasive histological biopsies. Single-cell RNA sequencing and T cell receptor (TCR) repertoire analysis of peripheral blood mononuclear cells (PBMCs) from matched liver transplant recipients before and after surgery revealed molecular signatures associated with acute rejection (AR). Patients who later developed AR exhibited distinct pre-operative immune states, including inflamed natural killer (NK) cells, clonally expanded effector memory CD8 T cells, and altered monocyte subsets. Following transplantation, these immune cells underwent rejection-specific reprogramming characterized by persistent pro-inflammatory activity and an enrichment of virus-specific CD8 T cells, despite immunosuppression. Five genes—CCL3, GZMK, MX1, RETN, and ATF3—were consistently upregulated in both pre- and post-operative AR samples. Among them, CCL3, GZMK, and MX1 were independently validated using a public large-scale liver biopsy dataset, confirming their roles in leukocyte recruitment, cytotoxicity, and antiviral response. RETN and ATF3were enriched in rejection-associated monocytes and functionally annotated as a secreted ligand and an activated transcription factor, respectively. These persistent gene signatures demonstrated strong predictive performance (AUC = 0.90) for AR. These findings provide a foundation for non-invasive risk stratification and early diagnosis of acute rejection, and highlight potential targets for personalized immunomodulatory therapy in liver transplantation.

Key words : Liver transplantation, Acute rejection, Single-cell RNA sequencing, Peripheral blood mononuclear cells

1. INTRODUCTION

Liver transplantation (LT) is the only effective treatment for patients with end-stage liver disease. Significant advances in surgical techniques and immunosuppressive therapies have markedly improved survival rates of transplant recipients[1]. Despite the liver's relative immune privilege compared to other transplanted organs, acute rejection occurs in approximately 15-30% of cases, representing a major complication that significantly impacts allograft survival[2,3]. Therefore, early detection and timely intervention for acute rejection are critical for optimizing transplant outcomes.

Histopathological assessment of liver biopsy specimens, interpreted through the rejection activity index (RAI), has traditionally been considered the gold standard for diagnosing acute rejection[4]. However, RAI scores do not consistently correlate with clinical deterioration of graft function[5,6], and this invasive procedure carries significant risks, particularly bleeding complications during the early post-transplant period[7]. These limitations underscore the need for complementary diagnostic approaches[8].

Elucidating the cellular and molecular alterations in the recipient's peripheral immune compartment is essential for identifying non-invasive early predictors of acute allograft rejection. However, comprehensive studies examining both pre- and post-transplant immunological phenotypes in patients who develop rejection remain limited[9–12]. Here, we identified predictive molecular signatures of acute allograft rejection through integrated single-cell RNA sequencing and T cell receptor (TCR) repertoire analysis on paired peripheral blood mononuclear cell (PBMC) samples collected from the same patients before and after transplantation.

2. MATERIALS AND METHODS

2.1 Experimental model and subject details

We performed case-control matched analyses using data from patients who underwent LT between May 2020 and December 2022 at Severance Hospital, Korea. The Inclusion criteria were adult patients (≥18 years) undergoing first-time liver transplantation. Exclusion criteria included multi-organ transplantation. PBMCs were prospectively collected at five time points: pre-LT, 1 week, 2 weeks, 1 month, and 2 months post-LT.

Acute rejection was defined by biopsy-proven rejection or clinical diagnosis. For six patients whose PBMCs were available within 3 days before acute rejection, control patients without rejection were matched at corresponding time points of acute rejection in a 1:1 manner. Patient matching was performed manually based on clinical variables previously reported in the literature associated with rejection. The variables were prioritized as follows: autoimmune hepatitis, retransplantation, ABO incompatibility, unrelated donor, donor age, and lymphocyte cross-matching. Each patient group was matched accordingly to ensure comparability and control for confounding factors. If multiple controls were available after matching the above variables, the following variables were considered: age, sex, HCC, pretransplant MELD, and BMI. A total of 24 samples from the 12 matched patients (6 AR, 6 NR) were analyzed, comprising 12 pre- and 12 post-operative samples.

The study was approved by the Institutional Ethics Committee (4-2016-0323), and all participants provided written informed consent. All patient clinical characteristics are shown in Table S1.

2.2 Method details

2.2.1 PBMC Isolation

PBMCs were isolated from whole blood using HISTOPAQUE-1077 (Sigma-Aldrich, St. Louis, MO) density gradient centrifugation. Briefly, blood was diluted 1:1 with phosphate-buffered saline (PBS; Gibco, Waltham, MA), layered over HISTOPAQUE, and centrifuged at 400 × g for 30 minutes at room temperature. Following centrifugation, the plasma layer was gently removed with a transfer pipet, and the PBMC layer at the interface was carefully transferred into a new conical tube. The PBMCs were subsequently washed twice with 40 mL of cold 2% fetal bovine serum (FBS) in PBS and centrifuged at 300 × g for 10 minutes at 4°C. Finally, the cells were cryopreserved using CELLBANKER 2 (Zenoaq Resource, Fukushima, Japan). Cryopreserved PBMCs were partially thawed rapidly at 37°C prior to use in analyses. The cells were carefully mixed with a washing medium (RPMI-1640 [Gibco] containing 20% FBS) in a dropwise manner to minimize osmotic shock. The volume was then adjusted to 10 mL with washing medium, and the cells were centrifuged at 300 × g for 10 minutes at room temperature. After centrifugation, the cell pellet was resuspended in 10 mL of washing medium, followed by cell counting. The cells were subsequently centrifuged again, and the resulting pellet was used for downstream analyses.

2.2.2 Bulk RNA sequencing and analysis

Thawed PBMCs were lysed in TRIzol reagent for RNA extraction and subsequent library preparation. RNA purification, cDNA library preparation, and sequencing were performed by Macrogen using the Illumina NovaSeq 6000 system. The raw FASTQ files were first processed by trimming reads using Trimmomatic (v0.39)[13], followed by alignment to the GRCh38 human reference genome (Ensembl release 98) with STAR (version 2)[14] and GENCODE v32 annotations. Gene-level read counts were generated using HTSeq-count (v0.11.2) with GENCODE v32 comprehensive annotations, including chromosomes, patches, haplotypes, and scaffolds. HTSeq-count was run in 'intersection-nonempty' mode, accounting for strand-specific information, with 'gene_id' as the feature ID and 'gene_name' as an additional attribute[15]. Differential gene expression analysis was performed using DESeq2[16]. For donor-specific variant references required for sample demultiplexing, aligned BAM files were processed according to the GATK 'SNP Calling from RNA-seq Data' pipeline[17].

2.2.3 10x Genomics and single cell sequencing

For the first sequencing set, pre- and post-operative samples were tagged by 1 µg BioLegend TotalSeq-C hashtag antibodies (C0251 and C0252, respectively) after Fc blocking by Human TruStain FcX (BioLegend, San Diego, CA). Cells were washed and suspended in 0.04% bovine serum albumin (BSA; Invitrogen, Waltham, MA) PBS solution. After the filtration through a 70 µm Flowmi cell strainer (Bel-Art SP, Wayne, NJ), samples were pooled and loaded on a Chromium X controller (10X Genomics , Pleasanton, CA). For the second set of sequencing, pre- and post-operative samples were separately loaded on GEM wells. For each set of experiments, approximately 70,000 cells per well were loaded into two wells of a Chromium Next GEM Chip K (10x Genomics). Sequencing libraries were generated using 10x Chromium Single Cell VDJ & 5' Gene Expression library and Gel Bead kits (10x Genomics) according to the manufacturer's protocol CG000330 Rev F. To produce hashtag antibody libraries, 0.2 µg of TotalSeq-C additive primer (Integrated DNA Technologies, Coralville, IA) was spiked in at the cDNA amplification step. Small size-selected amplified cDNA samples were used as templates for i7 indexing. Sequencing for Gene Expression, VDJ, and HTO libraries was performed on an Illumina NovaSeq 6000 system (Illumina, San Diego, CA).

2.2.4 Raw data processing

RNA and VDJ read alignment was performed using 10x Genomics Cell Ranger v7.1.0 with the 'multi' pipeline. Gene expression reads were aligned to the GRCh38 human reference genome (Ensembl release 98, 10x Genomics GRCh38-2020-A). For V(D)J analysis, reads were aligned to the GRCh38 human reference genome with alternative contigs and Ensembl V(D)J annotations (Ensembl release 98). We employed the CellBender algorithm for cell identification and count correction to mitigate background noise and enhance data quality[18].

2.2.5 Genetic variant-based donor demultiplexing

Donor IDs within the same sequencing pool were demultiplexed using Souporcell[19], utilizing genetic variant references derived from bulk RNA sequencing data of each patient. The demultiplexing process was performed using the Demuxafy pipeline[20]. The GRCh38 human reference genome (10x Genomics, 2020-A) was used as the reference sequence. A custom VCF file containing filtered minor allele frequency (MAF) > 10% variants was used for known genotypes.

The demultiplexing was performed on cell barcodes identified by CellBender, using the aligned BAM files from Cell Ranger output.

2.2.6 Quality control

To ensure the integrity of the cells used in downstream analysis, damaged or obsolete cells and genes were initially removed. Quality control was then applied by excluding cells that did not meet the following criteria: mitochondrial gene content < 20%; total UMI counts between 600 and 20,000 for the first dataset and between 1,000 and 20,000 for the second dataset; gene counts per cell between 400 and 5,000 for the first dataset and between 500 and 5,000 for the second dataset; hemoglobin gene content < 0.4%; and ribosomal gene content > 6%. Additionally, genes expressed in fewer than ten cells were filtered out to further refine the data.

2.2.7 Sample assignment through a hashtag

Hashtag reads were quantified as antibody expression using Cell Ranger. Sample assignment was performed on quality-controlled cell barcodes using the HTODemux [21] from the Seurat v4.3.0[22]. HTODemux was run with the following parameters: initialization with 3 clusters, a positive quantile threshold of 0.9, and the 'Clara' k-means clustering algorithm. The positive quantile threshold was adjusted to identify approximately 20-25% of cells as doublets, accounting for the intentional cell overloading during sample preparation. The random seed was set for reproducibility.

2.2.8 Preprocessing and multiplet removal

Following the normalization of cell counts by the median total counts, the data were log-transformed. Prior to multiplet removal, batch correction, and preliminary annotation were performed using scVI[23] and scANVI[24]. For this purpose, data from two QC-filtered sets were merged, and 3,161 highly variable genes (HVGs) common to the reference dataset (dbGaP: phs002315.v1.p1[22]) were selected using the 'highly_variable_genes' function from the Scanpy v1.9.3[25], specifically employing the 'seurat_v3' flavor. The model was initialized using scVI, with general model training conducted for 300 epochs. Individual sample IDs were used as batch keys for highly variable gene (HVG) selection and model setup. Subsequently, reference training with scANVI was carried out for 40 epochs, using 100 samples per label. Query data training was performed with 500 max epochs. Thirty latent space dimensions generated from this process were used to compute neighbors based on Euclidean distance. Leiden clustering with a resolution of 3.0 was then applied to the data. Among the 71 clusters identified, those with DoubletDetection[26] and Scrublet[27] scores exceeding 0.25 and 50, respectively, or predicted as doublets through the label transfer, were removed as potential doublets. These thresholds were determined after confirming actual doublet status through hashtag assignment and by validating the co-expression of markers from different cell types within each cluster. The final set of cells underwent reprocessing to ensure optimal downstream analysis. After the gene filtering, the top 2,000 HVGs were identified using the Seurat v3 method implemented in Scanpy Log-normalized counts were scaled to unit variance and zero mean, with a maximum value cap of 10.0. Principal Component Analysis (PCA) was performed on the scaled counts of HVGs. The Harmony algorithm was applied to the PCA results to correct batch effects, using the batch ID as the key for integration. A neighborhood graph was constructed using cosine distance in the Harmony-corrected latent space. Finally, Uniform Manifold Approximation and Projection (UMAP) was used for dimensional reduction and visualization of the data in two dimensions.

2.2.9 Enrichment analysis

Cellular processes and phenotypes were identified using gene set enrichment analysis (GSEA) through the prerank function of GSEApy[28]. For group comparisons in minor cell types, genes ranked by 'rank_genes_groups' in Scanpy using the Wilcoxon test with Benjamini-Hochberg correction were used as input. For major cell types, stat-ordered genes from the pseudo-bulk DEG analysis were utilized. Over-representation analysis for functional annotation of DEGs was conducted using gProfiler[29], with the ‘queries.enrich’ function from Scanpy. The activity of specific gene signatures was scored as the Area Under the Curve (AUC)[30]. User-defined genes below a specific percentile threshold are selected and ranked accordingly. Cumulative weights are then calculated based on this order. The AUC is computed as the weighted sum of rank differences and is normalized by dividing by the maximum possible AUC value.

2.2.10 Gene regulatory network analysis

SCENIC was used to reconstruct the gene regulatory network, with transcription factor (TF) enrichment and regulatory factor activity inferred through the pySCENIC pipeline[30]. A motif-based approach was employed, utilizing specific motif and rank files to refine regulons. The GRNBoost2 algorithm was applied for gene regulatory network inference, generating co-expression modules from the inferred adjacency matrix[31]. These modules were then pruned using the 'prune2df' function to evaluate the significance of each regulatory interaction. Cellular enrichment of each regulon was assessed using the AUCell algorithm, and the top regulon was identified based on the Regulon Specificity Score (RSS).

2.2.11 T cell receptor analysis

TCR analysis was conducted using Scirpy v0.13.1[32] and Muon v0.1.5[33]. Productive TCR chains and pairs were assessed with the 'index_chains' and 'chain_qc' functions. T cell clones were identified using the 'define_clonotypes' function based on primary TCR nucleotide identity, while clonotype clusters were determined with the 'define_clonotype_clusters' function, using amino acid alignment. Clonotype enrichment for each group was evaluated using the 'clonotype_imbalance' function. Clonotype alpha diversity was measured using the Gini index and normalized Shannon entropy. Additionally, epitope prediction for each clonotype was performed through alignment on VDJdb[34].

2.2.12 Classification model

For the classification model to assess the discriminatory potential of rejection-associated genes, we implemented a machine learning approach using logistic regression. Expression values were extracted from a public large-scale liver biopsy dataset (GSE145780) and standardized using z-score normalization. To ensure robust performance evaluation, we employed a 5-fold stratified cross-validation approach, maintaining consistent class distribution across all folds. The model performance was evaluated using receiver operating characteristic (ROC) curve analysis, with the area under the curve (AUC) as the primary metric. All analyses were performed using scikit-learn v1.3.0 in Python v3.10.13.`

2.2.13 Trajectory analysis

Pseudo-time calculation and trajectory inference were performed using scFates v1.0.6[35]. Initially, a target cell population was subsetted, and neighbors were defined in the harmony-corrected latent space. A diffusion map was constructed using Scanpy's 'tl.diffmap' function. Based on the specified diffusion map components, neighbor calculations, and Leiden clustering were carried out. A Partition-based Graph Abstraction (PAGA) graph was then created using the Fruchterman-Reingold algorithm, and the graph was visualized with Scanpy's 'tl.draw_graph'. Trajectory trees were constructed using the 'tl.tree' function from scFates with the Palantir Pseudotime Trajectories (PPT) method. The root tip was determined based on T cell naïve markers (CCR7, SELL, TCF7), and pseudo-time was calculated. Milestones, branches, and forks were defined, and genes associated with pseudo-time were fitted using the 'test_association' and 'tl.fit' functions. Finally, differentially expressed genes (DEGs) for each trajectory were identified using 'tl.test_fork'.

2.2.14 Cell-cell interaction analysis

Cell-cell interaction inference was performed using CellChat v1.5.0[36]. The anndata objects for each group were converted into CellChat objects, and signaling genes were identified using the 'identifyOverExpressedGenes' function. Interaction pairs were then determined based on the CellChatDB.human database, excluding non-protein signaling. Communication probability was calculated using the 'computeCommunProb' function with the triMean method, and pathways were inferred using the 'computeCommunProbPathway' function, considering only communications involving at least 10 cells.

2.3 Quantification and statistical analysis

For differential gene expression analysis, we used Memento v0.1.0[37] with a differential expression coefficient (de_coef) threshold of 0.5 and FDR-corrected p-value threshold of 0.05 for comparisons across groups. For four-group GSEA dot plots, top enriched pathways were selected using Normalized Enrichment Score (NES) >0 and FDR-corrected q-value <0.1. For Pre-NR versus Pre-AR enriched pathways dot plots, GSEA results with |NES| >0.5 and FDR-corrected q-value <0.1 were selected. For monocyte subpopulation top enriched pathway dot plots, |NES| >0.5 and FDR-corrected q-value <0.1 were used to adjust the number of pathways shown in plots. For gProfiler pathway visualization, we selected the top 10 or 15 pathways with g:GOSt-corrected p-value <0.01 and size <1500.

Cell type proportion in stacked bar plots within each group was not normalized. However, group proportions within specific subsets of cells were normalized by the total cell count of each group for that subset, enabling fair comparison between groups for subpopulations. When plotting density plots from the immune subtype level, cells from each group were subsampled to match the minimum cell count among groups, equalizing the total cell count in each density plot. For statistical testing of cell proportion bar plots, we used the Wilcoxon test for paired samples (within NR or AR groups) and Mann-Whitney test for unpaired samples (between NR and AR groups). For statistical analysis of liver biopsy bulk RNA expression data, the Mann-Whitney test was applied.

3. Results

3.1 Comprehensive Single-Cell Profiling Reveals Dynamic Immunological Changes Following Liver Transplantation

We collected paired pre- and post-operative PBMC samples from recipients who experienced acute rejection (Pre-AR or Post-AR; n = 6) and those who did not (Pre-NR or Post-NR; n = 6) (**Figure 1**). AR and NR cases were matched in pairs based on clinical parameters, such as age, gender, presence of hepatocellular carcinoma (HCC), autoimmune status, ABO compatibility, and donor age. In the AR group, post-operative samples were collected proximal to biopsy-confirmed or clinically diagnosed rejection episodes. Corresponding post-operative samples from the NR group were obtained at equivalent time points to enable direct comparative analysis.

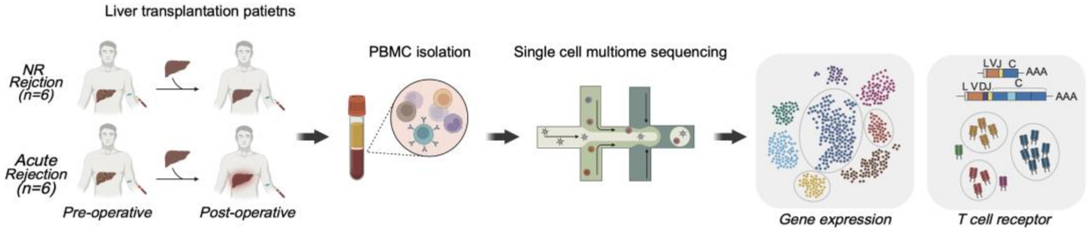

Figure 1. Schematic illustration of experimental design

We performed integrated single-cell RNA and TCR sequencing on a total of 24 samples, yielding 56,077 high-quality PBMCs after quality control filtering. Cells were initially categorized into eight major lineages—CD4 T cells, CD8 T cells, unconventional T cells, natural killer (NK) cells, monocytes, dendritic cells (DCs), B cells, and hematopoietic stem and progenitor cells (HSPCs)—based on canonical lineage marker expression (**Figure 2A, S1A, and S1B**). As illustrated in **Figure 2B**, both AR and NR samples exhibited substantial alterations in cellular distribution on UMAP dimensionality reduction. This transcriptional remodeling was further reflected in principal component analysis of pseudobulk profiles from individual samples (**Figure 2C**), highlighting the dramatic immunological dynamics induced following transplantation. Quantitative compositional analysis revealed distinct shifts in major immune cell populations between groups (**Figure 2D**). The NR group demonstrated a more pronounced expansion in monocyte proportions post-transplantation compared to the AR group. Conversely, the AR group maintained consistently higher proportions of CD8 T cells, despite their post-transplant reduction, and uniquely exhibited increased CD4 T cell frequencies after transplantation. Differentially expressed genes (DEGs) and subsequent gene set enrichment analysis revealed pre-transplant enrichment of T cell activation signatures and cytokine/chemokine networks in the Pre-AR group, while immunoglobulin-related pathways and antigen presentation mechanisms were overrepresented in the NR group (**Figure 2E and 2F**). Post-transplantation, both groups shared upregulation of blood vessel morphogenesis and apoptotic pathways, with more robust secretory granule activity in the NR group and enhanced pro-inflammatory cytokine responses in the AR group (**Figure 2F**).

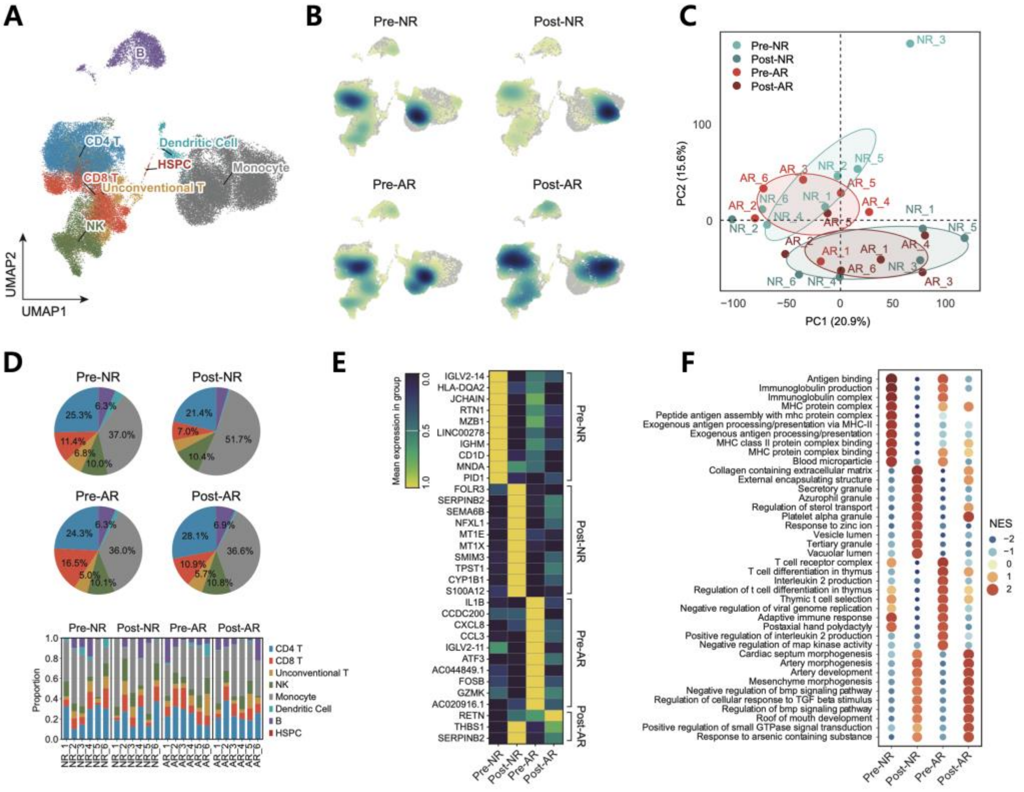

Figure 2. Comprehensive single-cell profiling in liver transplant recipients. A. UMAP visualization of major immune cell populations. **B**. Density plots showing relative cell distribution within each group using Gaussian kernel density estimation (scale 0-1). **C**. PCA plot of pseudobulk expression profiles for individual samples. **D.** Cellular composition analysis across groups (top) and individual samples (bottom). **E**. Heatmap of DEGs (de_coeff > 0.5, FDR-corrected p-value < 0.05) in each group with normalized expression values. **F**. Dot plot showing top 10 enriched pathways for each group identified by GSEA.

3.2 Pre-transplant Immune Activation Markers Associate with Rejection

We next delineated the molecular predisposition to rejection. Correlation analysis of gene expression fold changes following transplantation revealed general consistency between AR and NR groups (r = 0.68), but with distinct immunological signatures, as evidenced by the limited overlap of differentially expressed genes (DEGs) between groups (**Figure 3A**). We identified intrinsic transcriptional differences in the AR group before surgery, characterized by upregulation of 28 genes, including various chemokines/cytokines and effector/activation markers such as CD69, ATF3, GZMK, IL1B, CCL4, and CCL3 (**Figure 3B and S2C**), with distinct cellular sources for each (**Figure 3C**).

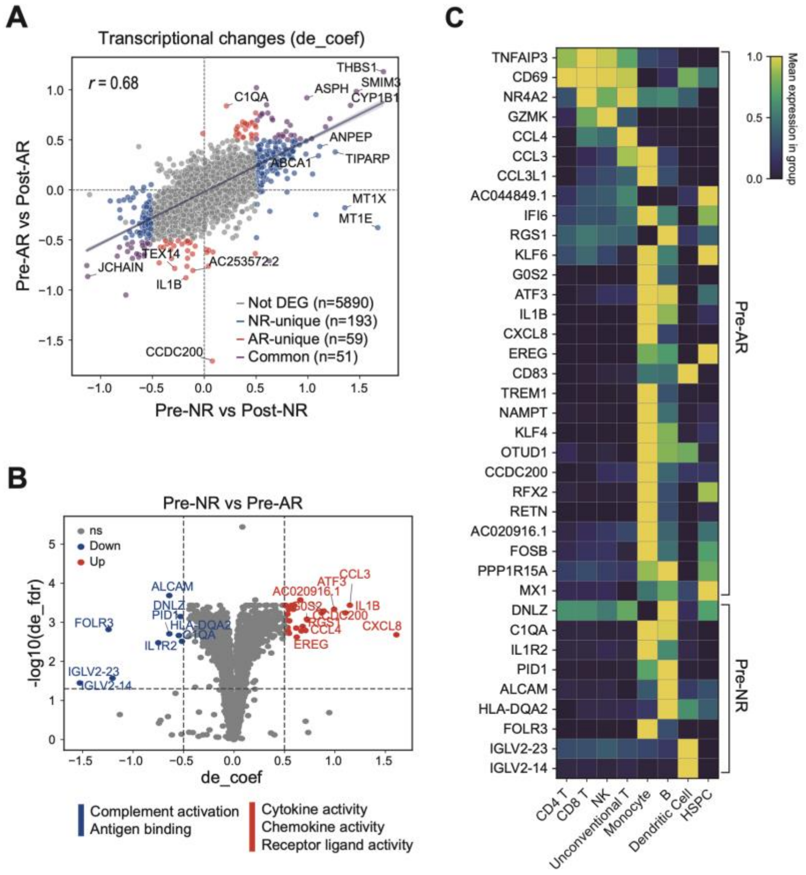

Figure 3. Differential gene expressions by rejection groups and immune cell types. A. Scatter plot showing correlation of post-transplant gene expression changes in NR (x-axis) and AR (y-axis) groups. Pearson correlation coefficient is indicated as r. **B.** Volcano plot displaying differential gene expression in Pre-AR compared to Pre-NR (de_coeff > 0.5, FDR-corrected p-value < 0.05). **C.** Heatmap illustrating cell type-specific expression patterns of pre-operative DEGs across major immune cell populations.

Notably, 5 of these 28 genes with known immune-activating functions remained consistently upregulated through the time of rejection (**Figure 4A**). To determine whether these peripheral blood transcriptional changes correlated with events at the site of rejection, we examined gene expression in liver biopsy specimens from rejection patients. This analysis confirmed the upregulation of CCL3, GZMK, and MX1 in the public bulk RNA-seq data of liver biopsy (**Figure 4B**), while the remaining genes (RETN and ATF3) may represent peripheral blood-specific features[38].

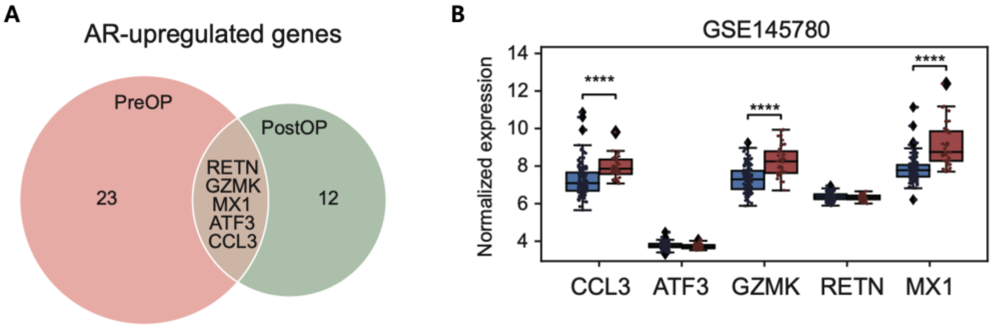

Figure 4. Genes upregulated in the AR group. A. Venn diagram showing the intersection between DEGs upregulated in AR in both pre- and post-operative samples. **B**. Expression in liver tissue biopsy bulk RNA-seq data. Statistical significance was determined using the Mann-Whitney test (****$p \leq 0.0001$).

Additionally, a rejection classification model incorporating these genes demonstrated an AUC of 0.90 (**Figure 5**), suggesting their potential utility as non-invasive biomarkers for predicting or diagnosing acute rejection.

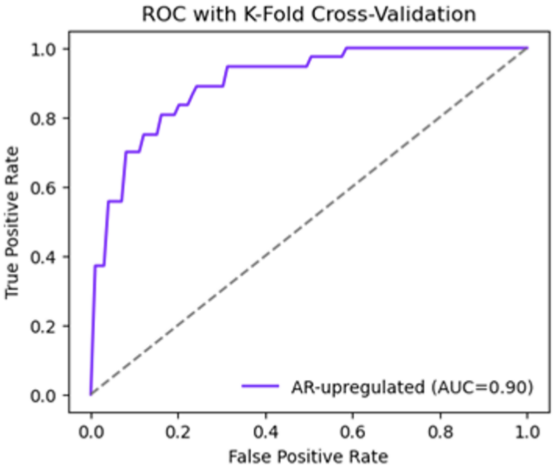

Figure 5. ROC curve for rejection decision model using liver biopsy bulk RNA data

(GSE145780)

Cell type-specific comparison between Pre-NR and Pre-AR samples revealed that the predisposed differences in immune-related pathways were primarily derived from NK cells, T cells, and monocytes (**Figure 6**). Although monocytes in the Pre-AR group exhibited diminished antigen presentation capacity and reduced energy metabolism (oxidative phosphorylation and TCA cycle activity; **Figure 6**), post-transplant antigen presentation-related genes were significantly upregulated in the AR group, suggesting that monocyte function becomes fully activated during the rejection process.

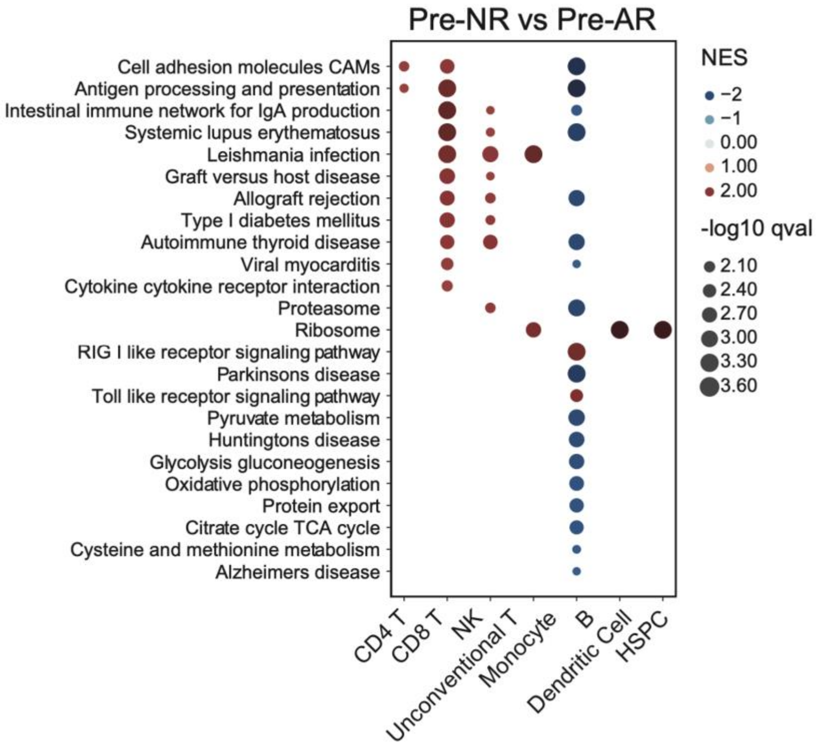

Figure 6. Enriched molecular pathways in Pre-AR samples across different cell types.

3.3 NK Cell Subsets Show Distinct Inflammatory and Migratory Features in Pre-Rejection States

Moving beyond gene marker analysis, we sought to characterize predisposed immune heterogeneity at the cellular subtype level. We performed in-depth analysis of NK and T cells, which exhibited activated phenotypes in Pre-AR samples (**Figure 6**), by conducting detailed subtype annotation (**Figure 7A**). Quantitatively, both AR and NR groups demonstrated a decrease in central memory populations and an increase in naïve populations within CD4 and CD8 T cell compartments (**Figure 7B**). NK cells showed a significant increase exclusively in the NR group. To examine qualitative differences in NK cells, we classified them into four distinct clusters based on marker gene expression (**Figure 7C**).

As a shared feature induced by surgery, both groups exhibited increased proportions of NK_injury cells, characterized by elevated expression of platelet-related genes (**Figure 7D and 3E**). Meanwhile, the NR group consistently maintained higher proportions of NK_adaptive cells, which are characterized by extended longevity and memory phenotype[39,40] (**Figure 7F**). In contrast, the AR group had a higher pre-operative proportion of NK_CD56bright and NK_terminal clusters. Although NK_terminal cells exhibited cytotoxicity gene scores comparable to NK_adaptive cells they displayed activated chemokine signaling and, together with NK_CD56bright cells, showed elevated scores for inflamed NK signature, IFNγ response, and migration potential (**Figure 7F**). Post-operatively, the proportion of NK_CD56bright and NK_terminal cells decreased in the AR group, yet NK stimulation via IFN-γ signaling remained sustained after surgery (**Figure 7F and 3G**).

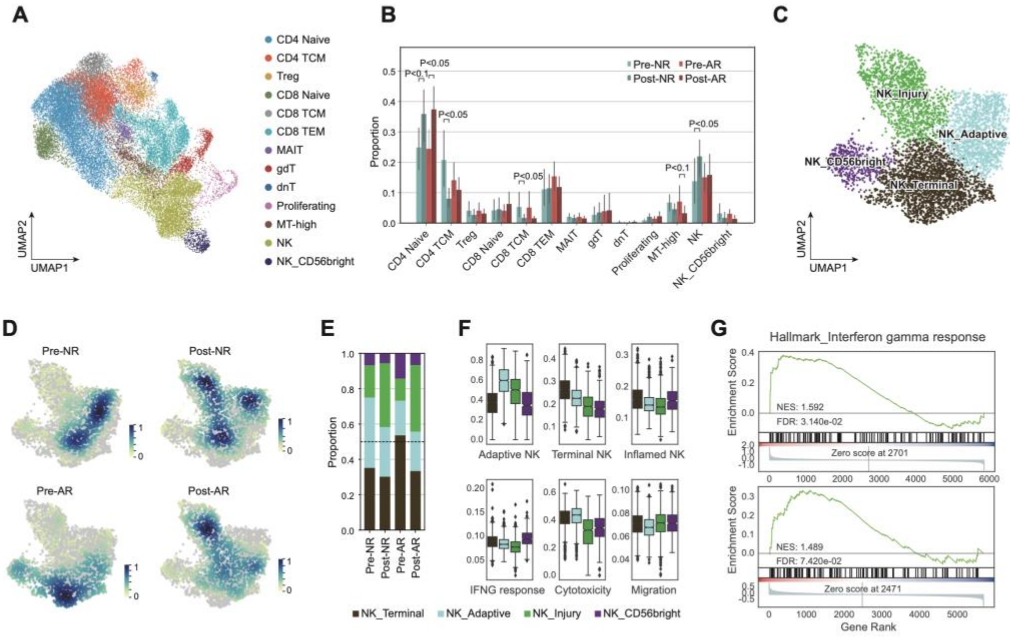

Figure 7. Pre-operative T and NK cell modulation in acute rejection. A. UMAP visualization of NK and T cell subtypes. **B.** Bar plots showing proportions of NK and T cell subtypes across groups. Statistical significance was determined using Wilcoxon test for paired samples (within NR or AR)

and Mann-Whitney test for unpaired samples (between NR and AR). **C**. UMAP visualization of NK cell subpopulations. **D**. Density plots showing NK cell distribution across groups, with cells subsampled to equal numbers for comparable visualization. **E**. Stacked bar plot showing the relative proportions of subpopulations within NK cells. **F**. Gene set scores for each NK cell subpopulation. **G**. Enrichment plots comparing interferon γ response pathways between NR versus AR groups Pre- (top) and post-transplantation (bottom).

3.4 CD8 T Cell Clonal Dynamics Reveal Different Evolutionary Paths in Rejection versus Non-Rejection

For T cells, we performed TCR analysis to investigate whether clonal expansion contributed to graft rejection (**Figure 8A**). While both groups showed decreased clonality post-transplantation, the AR group consistently maintained higher clonality compared to the NR group (**Figure 8B**). Notably, examination of the top 10 clonotypes by clone size revealed that they were almost exclusively specific to either the AR or NR group, with the majority belonging to the effector memory CD8 T cell (CD8 TEM) compartment (**Figure 8C**). To determine whether these dominant clonotypes in AR and NR groups represented distinct phenotypic populations, we analyzed their distribution across CD8 T cell clusters.

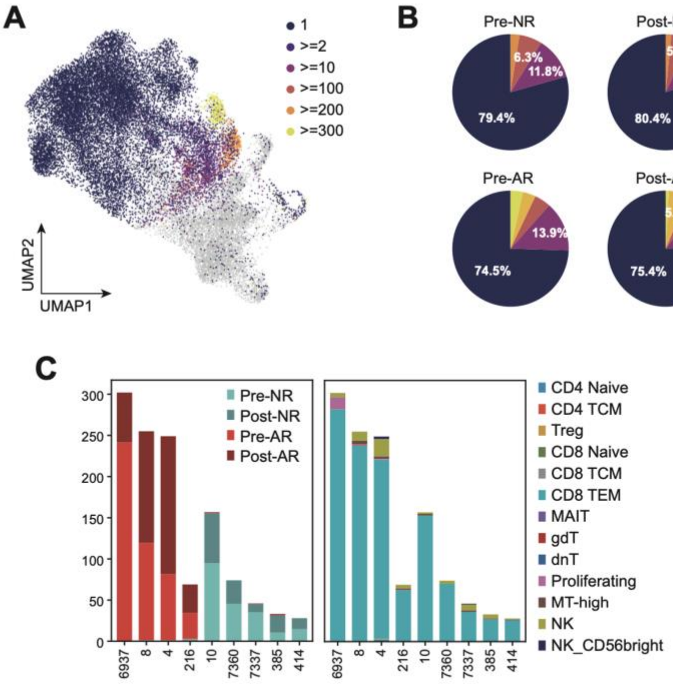

Figure 8. Clonotype size distribution across NK and T cell subsets. A. UMAP plot showing clonotype size distribution across NK and T cell subsets. **B.** Distribution of clonotype sizes in each experimental group. **C.** Group (left) and subtype composition (right) of the top 10 clonotypes. Group compositions were normalized by cell counts of each group.

Effector memory CD8 T cells were further subdivided into five populations based on marker gene expression (**Figure 9A, and S4C**). Among these, CD8 TEM_IL7R cells, which express progenitor-exhausted T cell (Tpex) markers such as GZMK and IL-7R, were uniformly distributed across all groups (**Figure 9B and 9C**). Consistent with known Tpex characteristics, these cells exhibited relatively low cytotoxicity and moderate expression of coinhibitory molecules (**Figure 9D**). Their low clonality suggests that they are a population composed of diverse, newly differentiating clones.

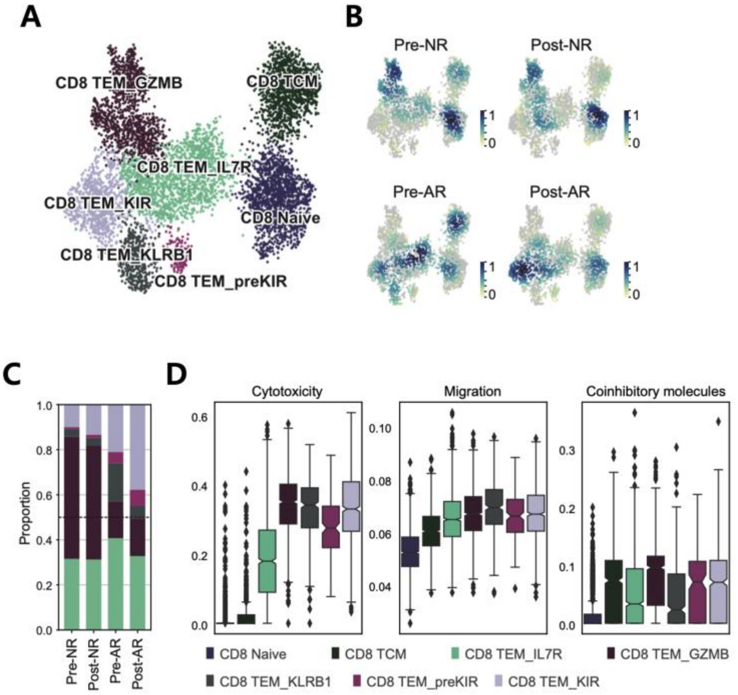

Figure 9. CD8 T cell distribution and gene set score by clonotypes. A. UMAP visualization of CD8 T cell subpopulations. **B.** Density plots showing CD8 T cell distribution across groups, with cells subsampled to equal numbers for comparable visualization. **C.** Stacked bar plot showing the relative proportions of subpopulations within CD8 T cells. **D.** Gene set scores for each CD8 T cell subpopulation.

Interestingly, nearly half of the effector memory CD8 T cells in the NR group were classified as CD8 TEM_GZMB, characterized by expression of potent cytotoxicity genes such as

GNLY and GZMB, and these cells constituted all top clonotypes in the NR group (**Figure 9A**). However, their high inhibitory molecule score and stable proportions before and after surgery suggest they represent pre-existing chronic memory populations in the recipients (**Figure 9C and 9D**)

In contrast, the AR group exhibited markedly elevated levels of CD8 TEM_KLRB1 cells before surgery compared to other groups (**Figure 9C**). The protein product of KLRB1, CD161, is a marker for T cells with tissue-homing capacity, and previous studies have reported that CD8 T cells expressing this marker display reduced susceptibility to immune exhaustion. Consistent with these reports, this cluster maintained high cytotoxicity comparable to CD8 TEM_GZMB cells while exhibiting substantially lower expression of coinhibitory molecules (**Figure 9D**). Similar to the aforementioned migratory and inflamed NK cell (**Figure 7E**), this cluster not only exhibited the highest migratory score among effector memory CD8 T cell clusters but also showed a dramatic reduction following surgery (**Figure 9C and 9D)**. The remaining two clusters were predominantly distributed in the AR group (**Figure 9B)** and uniquely exhibited increased clonotype sizes and proportions following surgery (**Figure 8C and 9C**).

3.5 Monocytes Display Transcriptomic Divergence and Pro-Inflammatory Signatures in Acute Rejection

Monocytes, which play crucial roles in innate immunity and transplant responses, represented a substantial proportion of cells in our dataset. Given their importance in antigen presentation and inflammatory regulation during allograft rejection, we performed comprehensive characterization of monocyte heterogeneity and functional states. Monocytes are commonly categorized into CD14-expressing classical monocytes (CD14 Mono) and CD16-expressing non-classical monocytes (CD16 Mono) (**Figure 10A**). CD14 Mono clusters were further classified into two subpopulations: CD14 Mono_IL1B and CD14 Mono_RNASE2, each with distinct marker expression profiles (**Figure 10B**). The remaining CD14 Mono population exhibited elevated expression of mitochondrial and ribosomal genes. We observed conserved patterns of monocyte dynamics in both AR and NR groups. Both showed a decrease in CD14 Mono_IL1B and an increase in CD14 Mono_RNASE2 following transplantation (**Figure 10C and 10D**).

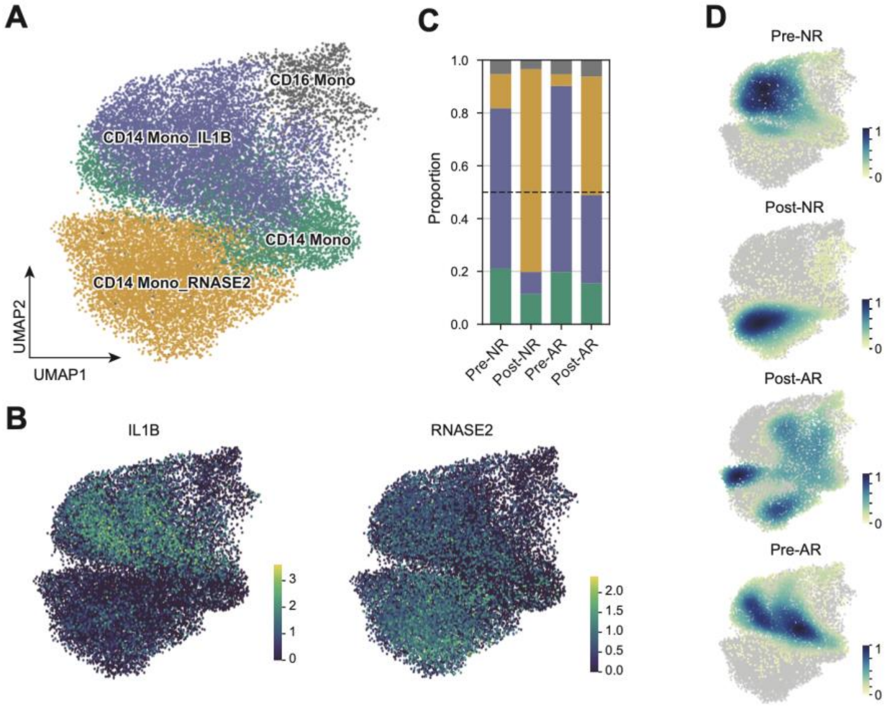

Figure 10. Distribution of monocytes subpopulations. A. UMAP visualization of monocyte subpopulations. **B.** UMAP highlighting marker gene expression across monocyte subsets. **C.** Stacked bar plot showing the relative proportions of subpopulations within monocytes. **D**. Density plots showing monocyte distribution across groups, with cells subsampled to equal numbers for comparable visualization.

Interestingly, the CD14 Mono_IL1B population, which was predominant before surgery, exhibited enhanced inflammatory signaling including interferon and TNF-α pathways (**Figure 11**), as well as elevated expression of genes related to monocyte differentiation and antigen-presenting cell function compared to other populations (**Figure 12**). Conversely, the post-surgically expanded Mono_RNASE2 population was enriched for pathways associated with OXPHOS, glycolysis, ROS response, and vascular repair and fibrosis—processes integral to post-surgical recovery (**Figure 11**). This cellular transition likely reflects comprehensive effects of post-surgical monocyte reprogramming and immunosuppressive therapy.

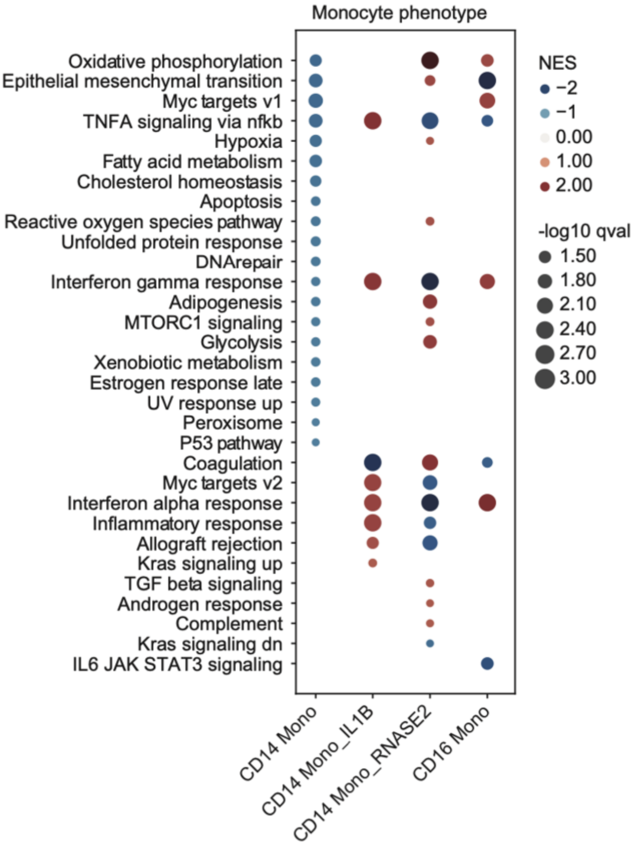

Figure 11. Enriched molecular pathways in each monocyte subpopulation.

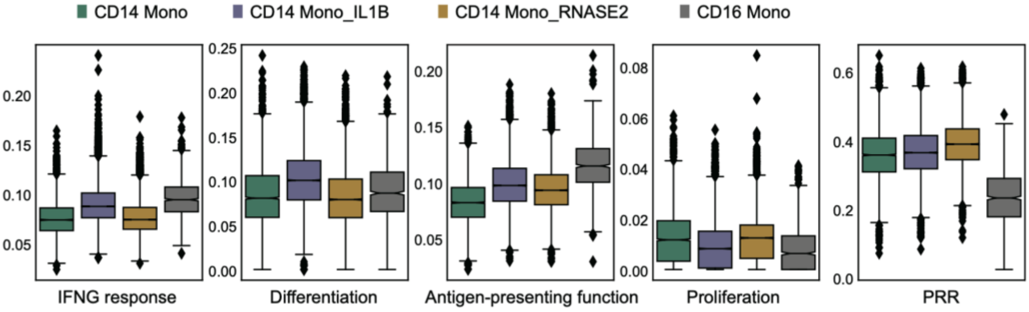

Figure 12. Gene set scores for each monocyte subpopulation.

These findings align with previous studies reporting a post-transplant decline in monocyte antigen-presenting capacity and differentiation potential, accompanied by increased pattern recognition receptor (PRR) expression and proliferation during the early recovery phase—characteristics exhibited by the CD14 Mono_RNASE2 population (**Figure 12**). Furthermore, this study identified RNASE2-expressing monocytes and secreted RNASE2 as potential indicators of immune tolerance in the post-transplant setting. Regulon activity analysis revealed that ATF3, a transcription factor consistently upregulated in AR group (**Figure 4A**), was predominantly expressed and activated in CD14 Mono_IL1B (**Figure 13A and 13B**). Given that ATF3 is known to exert dual roles in either promoting or suppressing immune responses, its precise function in inflammatory monocytes—whether it amplifies inflammation or serves as a negative feedback regulator—requires further investigation.

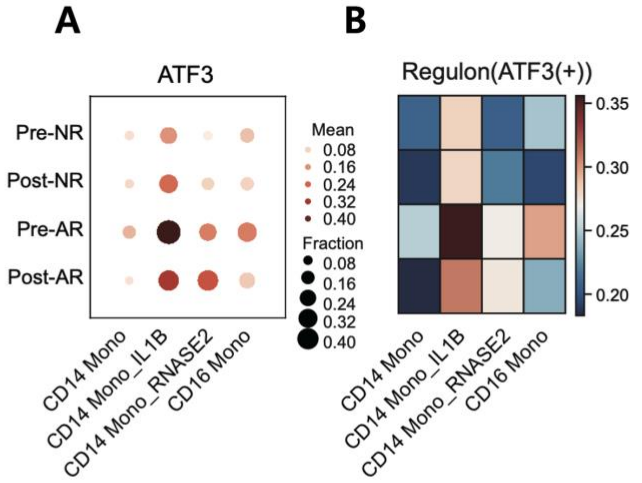

Figure 13. Transcriptional activity of ATF3 in each subpopulation of monocyte. A. Mean expression of ATF3 by group and monocyte subpopulation. **B**. Transcriptional activity of ATF3 by group and monocyte subpopulation.

3.6 Cell-Cell Interaction Networks Maintain Higher Activity in Rejection Cases

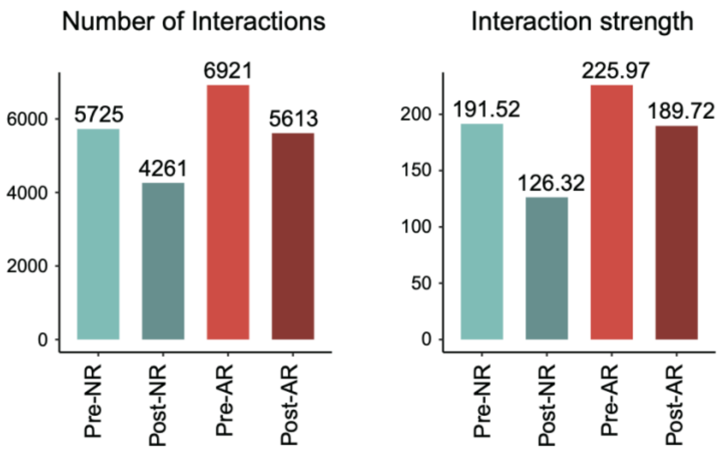

Figure 14. Number and strength of cell-cell interactions detected per group

To assess the overall immune cell interactions based on the previously identified phenotypic differences, we performed cell-cell interaction (CCI) analysis. Both NR and AR groups exhibited a reduction in the number and strength of CCIs after surgery, likely as a consequence of high-dose immunosuppressant therapy (**Figure 14**). However, the AR group consistently maintained higher interaction intensity, suggesting sustained immune cell activity despite immunosuppression. Comparison of cell type contributions to signaling networks revealed that CD8 TEM_KLRB1, CD8 TEM_preKIR, and CD8 TEM_KIR—clusters previously highlighted in the AR group—exhibited the most pronounced differences (**Figure 15**), primarily driven by the enhanced activation of ICAM and PAR, CLEC, and MHC-I signaling pathways, respectively (**Figure S6A-S6C**). These findings support the central role of these clusters in allograft rejection.

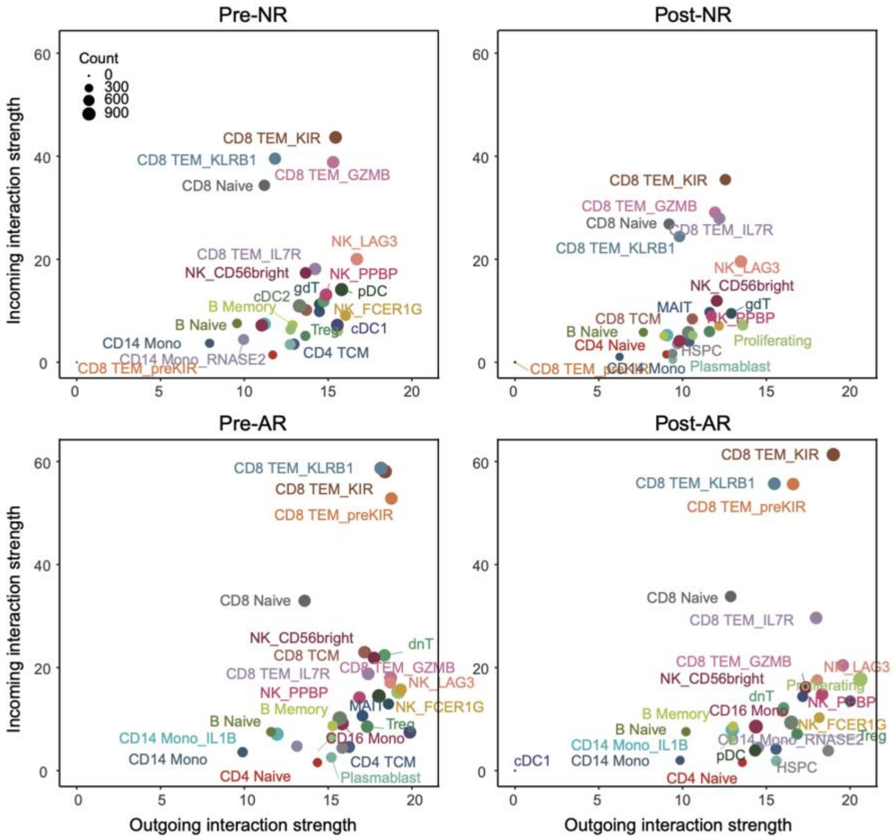

Figure 15. interaction strength of receptors and ligands by cell types

Additionally, we previously identified monocytes as the cellular source of RETN (resistin), a DEG marker in the AR group (**Figure 2C**). Further analysis revealed CD14 Mono_RNASE2 as the main resistin-expressing population (**Figure 6SD**) and confirmed its involvement in cell-cell interactions with T cells and NK cells, particularly before surgery (**Figure 16**). This suggests that the functional differences within tissue recovery-associated monocyte populations, rather than inherently pro-inflammatory CD16 Mono or CD14 Mono_IL1B subsets, may serve as potential predictors of rejection.

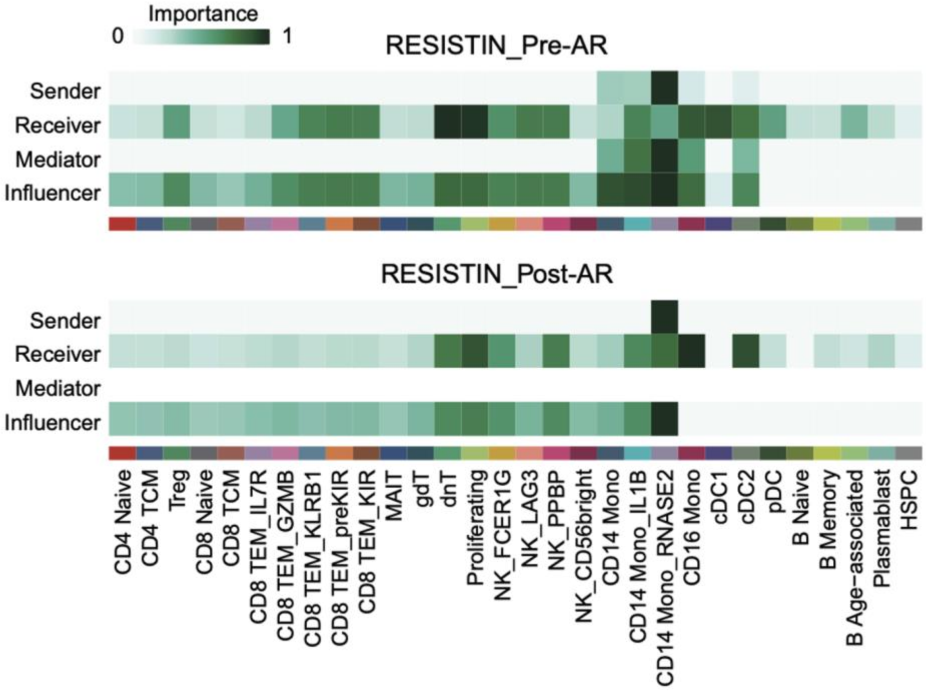

Figure 16. Relative importance of the RESISTIN interaction network by each cell types in AR group.

4. DISCUSSION

Despite the extensive application of single-cell analysis in transplantation research, most studies have predominantly focused on post-operative samples, with limited efforts to identify predictive markers for rejection before surgery[10–12,41,42]. In this study, we investigated the immune landscape of acute rejection by performing comprehensive single-cell transcriptomic analysis of PBMCs from liver transplant recipients. Using genetic multiplexing to efficiently process multiple samples, we uniquely analyzed paired pre- and post-transplant samples from the same patients, enabling direct comparison of immune states before and after rejection onset. Our findings reveal distinct pre-operative immune signatures and post-operative immune reprogramming patterns that may contribute to allograft rejection.

Pre-operatively, AR patients exhibited an activated immune profile, with increased NK_CD56bright and NK_terminal subsets showing enhanced cytotoxicity and pro-inflammatory signaling. Their elevated IFN-γ response and migration potential suggest a predisposition to rejection. The post-operative decline in these subsets indicates their involvement in graft-directed immune responses, though further validation is needed to determine their fate post-transplantation.

TCR repertoire analysis highlighted distinct clonal expansion dynamics in AR patients, who maintained higher clonality post-operatively. AR-associated clonotypes were enriched in CD8 TEM_KLRB1, CD8 TEM_preKIR, and CD8 TEM_KIR clusters. TEM_KLRB1, predominant in pre-AR samples, exhibited high cytotoxicity and low inhibitory molecule expression, suggesting a migratory and persistent effector phenotype. Its branching marker, CORO1A, is crucial for alloreactive T cell survival, with studies suggesting its inhibition could promote tolerance[43]. If CD8 TEM_KLRB1 cells represent cross-reactive alloreactive T cells infiltrating the graft to trigger rejection, CORO1A inhibition might offer a highly specific suppression strategy.

Post-transplantation, CD8 TEM_KIR emerged as the dominant subset, exhibiting strong inflammatory signatures linked to IRF1 and TYROBP activation. This population also exhibited virus-specificity together with CD8 TEM_preKIR, an intermediate population in its phenotypic transition. The post-transplant expansion of these populations suggests that pre-existing virus-specific memory T cells may be non-canonically stimulated in the allograft rejection context, leading to bystander T cell formation. Bystander T cells are known to express NK receptors such as KIR, and their involvement in allograft rejection has been reported in heart transplantation[44,45]. Our findings provide a basis for investigating whether similar mechanisms occur in liver transplantation. These results indicate that CD8 T cells in AR patients undergo a phenotypic shift from Pre- transplant migratory effector states toward a post-transplant inflammatory and cytotoxic profile, potentially driving rejection events.

Monocyte subtypes also demonstrate distinct transcriptomic reprogramming following transplantation. Both AR and NR groups exhibited a shift from inflammatory CD14 Mono_IL1B to CD14 Mono_RNASE2. Notably, reduced expansion of CD14 Mono_RNASE2 and persistent FOS-expressing inflammatory monocytes have been linked to acute cellular rejection in liver transplantation, suggesting that monocyte reprogramming could serve as an indicator of graft acceptance[11].

Cell-cell interaction analysis revealed reduced interaction strength in both groups post-transplantation, likely due to immunosuppression. However, AR patients maintained higher interaction intensity, reflecting sustained immune activation. Key contributors included CD8 TEM_KLRB1, CD8 TEM_KIR, and CD8 TEM_preKIR, which exhibited enhanced antigen presentation and cytotoxic signaling. Additionally, we identified CD14 Mono_RNASE2 as the primary source of RETN, an intrahepatic cytokine associated with liver inflammation and fibrosis[46]. This suggests that immune divergence between AR and NR is not solely driven by inflammatory monocytes (e.g., CD14 Mono_IL1B) but may also involve tissue-repairing monocyte subsets with differential signaling properties.

Furthermore, we identified five consistently upregulated genes (CCL3, GZMK, MX1, RETN, ATF3) in both pre- and post-operative AR samples. Three of these genes (CCL3, GZMK, MX1)—linked to leukocyte recruitment, cytotoxicity, and antiviral responses [47–50]—were also confirmed to be significantly upregulated in a public large-scale liver biopsy dataset. The remaining genes (RETN and ATF3) were confirmed to be functionally relevant as an activated transcription factor and secreted ligand in rejection-associated monocytes. These persistent signatures demonstrated strong discriminatory potential (AUC=0.90), highlighting their biological relevance throughout the transplantation process and potential utility for clinical rejection risk assessment.

While PBMC analysis provides a window into systemic immune responses rather than directly capturing events at the graft site, identifying robust peripheral biomarkers has significant clinical advantages. The distinct cellular subsets we identified—particularly CD8 TEM_KLRB1, CD8 TEM_KIR, and CD14 Mono_RNASE2—represent promising candidates for stratifying recipients at risk of rejection. Future studies incorporating spatial transcriptomics and graft-infiltrating immune cell profiling will complement our findings by further delineating their precise contributions at the graft site.

5. CONCLUSION

This study identified distinct peripheral immune signatures predictive of acute rejection before and after liver transplantation, including persistently upregulated genes such as CCL3, GZMK, MX1, RETN, ATF3. These findings highlight the potential of PBMC-based transcriptomic profiling as a non-invasive tool for early rejection risk assessment and future personalized immunotherapy.

REFERENCES

1. Kwong AJ, Ebel NH, Kim WR, et al. OPTN/SRTR 2020 Annual Data Report: Liver. American Journal of Transplantation. 2022;22(S2):204-309.
2. Jadlowiec CC, Morgan PE, Nehra AK, et al. Not All Cellular Rejections Are the Same: Differences in Early and Late Hepatic Allograft Rejection. Liver Transpl. 2019;25(3):425-435.
3. Levitsky J, Goldberg D, Smith AR, et al. Acute Rejection Increases Risk of Graft Failure and Death in Recent Liver Transplant Recipients. Clin Gastroenterol Hepatol. 2017;15(4):584-593.e582.
4. Demetris AJ, Batts KP, Dhillon AP, et al. Banff schema for grading liver allograft rejection: an international consensus document. Hepatology (Baltimore, Md.). 1997;25(3):658-663.
5. Bartlett AS, Ramadas R, Furness S, Gane E, McCall JL. The natural history of acute histologic rejection without biochemical graft dysfunction in orthotopic liver transplantation: A systemic review. Liver Transplantation. 2002;8(12):1147-1153.
6. Höroldt BS, Burattin M, Gunson BK, et al. Does the Banff rejection activity index predict outcome in patients with early acute cellular rejection following liver transplantation? Liver

Transplantation. 2006;12(7):1144-1151.

7. Alturkistani H, Alsergani AH, Alzeer M, Alturkistani A, Zaini R, Bauones S. Ultrasound-guided percutaneous liver biopsy: A review of what operators need to know. Medicine (United States). 2024;103(30):e38673-e38673.
8. Taner T, Bruner J, Emamaullee J, Bonaccorsi-Riani E, Zarrinpar A. New Approaches to the Diagnosis of Rejection and Prediction of Tolerance in Liver Transplantation. Transplantation. 2022;106(10):1952-1962.
9. Alachkar H, Mutonga M, Kato T, et al. Quantitative characterization of T-cell repertoire and biomarkers in kidney transplant rejection. BMC Nephrology. 2016;17(1):1-9.
10. Liu Y, Hu J, Liu D, et al. Single-cell analysis reveals immune landscape in kidneys of patients with chronic transplant rejection. Theranostics. 2020;10(19):8851-8862.
11. Wang R, Peng X, Yuan Y, et al. Dynamic immune recovery process after liver transplantation revealed by single-cell multi-omics analysis. Innovation. 2024;5(3).
12. Li X, Li S, Wu B, et al. Landscape of Immune Cells Heterogeneity in Liver Transplantation by Single-Cell RNA Sequencing Analysis. Frontiers in Immunology. 2022;13:890019-890019.
13. Madill-Thomsen K, Abouljoud M, Bhati C, et al. The molecular diagnosis of rejection in liver transplant biopsies: First results of the INTERLIVER study. American Journal of Transplantation. 2020;20(8):2156-2172.
14. Corat MAF, Schlums H, Wu C, et al. Acquired somatic mutations in PNH reveal long-term maintenance of adaptive NK cells independent of HSPCs. Blood. 2016;129(14):1940-1940.
15. Basílio-Queirós D, Venturini L, Luther-Wolf S, et al. Adaptive NK cells undergo a dynamic modulation in response to human cytomegalovirus and recruit T cells in in vitro migration assays. Bone Marrow Transplantation 2022 57:5. 2022;57(5):712-720.
16. Wang Z, Shao X, Wang K, et al. Single-cell analysis reveals a pathogenic cellular module 1 associated with early allograft dysfunction after liver 2 transplantation.
17. Shi T, Burg AR, Caldwell JT, et al. Single-cell transcriptomic analysis of renal allograft rejection reveals insights into intragraft TCR clonality. Journal of Clinical Investigation. 2023;133(14).
18. Jayachandran R, Gumienny A, Bolinger B, et al. Disruption of Coronin 1 Signaling in T Cells Promotes Allograft Tolerance while Maintaining Anti-Pathogen Immunity. Immunity. 2019;50(1):152-165.e158.
19. Kim TS, Shin EC. The activation of bystander CD8+ T cells and their roles in viral infection. Experimental & Molecular Medicine 2019 51:12. 2019;51(12):1-9.
20. Khorki ME, Shi T, Cianciolo EE, et al. Prior viral infection primes cross-reactive CD8+ T cells that respond to mouse heart allografts. Frontiers in Immunology. 2023;14:1287546-1287546.
21. Bertolani C, Sancho-Bru P, Failli P, et al. Resistin as an Intrahepatic Cytokine: Overexpression during Chronic Injury and Induction of Proinflammatory Actions in Hepatic Stellate Cells. The American Journal of Pathology. 2006;169(6):2042-2053.
22. Honey K. CCL3 and CCL4 actively recruit CD8+ T cells. Nature Reviews Immunology 2006 6:6. 2006;6(6):427-427.

23. Kang TG, Park HJ, Moon J, Lee JH, Ha SJ. Enriching CCL3 in the Tumor Microenvironment Facilitates T cell Responses and Improves the Efficacy of Anti-PD-1 Therapy. Immune Network. 2021;21(3).

24. Henkart PA, Sitkovsky MV. Cytotoxic Lymphocytes: Two ways to kill target cells. Current Biology. 1994;4(10):923-925.

25. Verhelst J, Parthoens E, Schepens B, Fiers W, Saelens X. Interferon-Inducible Protein Mx1 Inhibits Influenza Virus by Interfering with Functional Viral Ribonucleoprotein Complex Assembly. Journal of Virology. 2012;86(24):13445-13455.

26. Bolger AM, Lohse M, Bioinformatics BU, undefined. Trimmomatic: a flexible trimmer for Illumina sequence data. academic.oup.comAM Bolger, M Lohse, B UsadelBioinformatics, 2014•academic.oup.com. 2014;30(15):2114-2120.

27. Dobin A, Davis CA, Schlesinger F, et al. STAR: ultrafast universal RNA-seq aligner. academic.oup.comA Dobin, CA Davis, F Schlesinger, J Drenkow, C Zaleski, S Jha, P Batut, M ChaissonBioinformatics, 2013•academic.oup.com. 2013;29(1):15-21.

28. Anders S, Pyl PT, bioinformatics WH, undefined. HTSeq—a Python framework to work with high-throughput sequencing data. academic.oup.com. 2015;31(2):166-169.

29. Love MI, Huber W, Anders S. Moderated estimation of fold change and dispersion for RNA-seq data with DESeq2. Genome Biology. 2014;15(12):1-21.

30. Van der Auwera GA, Carneiro MO, Hartl C, et al. From fastQ data to high-confidence variant calls: The genome analysis toolkit best practices pipeline. Current Protocols in Bioinformatics. 2013(SUPL.43).

31. Fleming SJ, Chaffin MD, Arduini A, et al. Unsupervised removal of systematic background noise from droplet-based single-cell experiments using CellBender. Nature Methods 2023 20:9. 2023;20(9):1323-1335.

32. Heaton H, Talman AM, Knights A, et al. Souporcell: robust clustering of single-cell RNA-seq data by genotype without reference genotypes. Nature Methods 2020 17:6. 2020;17(6):615-620.

33. Neavin D, Senabouth A, Lee JTH, et al. Demuxafy: Improvement in droplet assignment by integrating multiple single-cell demultiplexing and doublet detection methods. bioRxiv. 2022;5:2022.2003.2007.483367-482022.483303.483307.483367.

34. Stoeckius M, Zheng S, Houck-Loomis B, et al. Cell Hashing with barcoded antibodies enables multiplexing and doublet detection for single cell genomics. Genome Biology. 2018;19(1):1-12.

35. Hao Y, Hao S, Andersen-Nissen E, et al. Integrated analysis of multimodal single-cell data. Cell. 2021;184(13):3573-3587.e3529.

36. Lopez R, Regier J, Cole MB, Jordan MI, Yosef N. Deep generative modeling for single-cell transcriptomics. Nature Methods 2018 15:12. 2018;15(12):1053-1058.

37. Xu C, Lopez R, Mehlman E, Regier J, Jordan MI, Yosef N. Probabilistic harmonization and annotation of single-cell transcriptomics data with deep generative models. Molecular Systems Biology. 2021;17(1):9620-9620.

38. Wolf FA, Angerer P, Theis FJ. SCANPY: large-scale single-cell gene expression data

analysis. Genome Biology. 2018;19(1):15-15.

39. JonathanShor/DoubletDetection: doubletdetection v4.2.

40. Wolock SL, Lopez R, Klein AM. Scrublet: Computational Identification of Cell Doublets in Single-Cell Transcriptomic Data. Cell Systems. 2019;8(4):281-291.e289.

41. Fang Z, Liu X, Peltz G. GSEApy: a comprehensive package for performing gene set enrichment analysis in Python. Bioinformatics. 2023;39(1).

42. Kolberg L, Raudvere U, Kuzmin I, Adler P, Vilo J, Peterson H. g:Profiler—interoperable web service for functional enrichment analysis and gene identifier mapping (2023 update). Nucleic Acids Research. 2023;51(W1):W207-W212.

43. Aibar S, González-Blas CB, Moerman T, et al. SCENIC: single-cell regulatory network inference and clustering. Nature Methods 2017 14:11. 2017;14(11):1083-1086.

44. Moerman T, Aibar Santos S, Bravo González-Blas C, et al. GRNBoost2 and Arboreto: efficient and scalable inference of gene regulatory networks. Bioinformatics. 2019;35(12):2159-2161.

45. Sturm G, Szabo T, Fotakis G, et al. Scirpy: a Scanpy extension for analyzing single-cell T-cell receptor-sequencing data. Bioinformatics. 2020;36(18):4817-4818.

46. Bredikhin D, Kats I, Stegle O. MUON: multimodal omics analysis framework. Genome Biology. 2022;23(1):1-12.

47. Bagaev DV, Vroomans RMA, Samir J, et al. VDJdb in 2019: database extension, new analysis infrastructure and a T-cell receptor motif compendium. Nucleic Acids Research. 2020;48(D1):D1057-D1057.

48. Faure L, Soldatov R, Kharchenko PV, Adameyko I. scFates: a scalable python package for advanced pseudotime and bifurcation analysis from single-cell data. Bioinformatics. 2023;39(1).

49. Jin S, Guerrero-Juarez CF, Zhang L, et al. Inference and analysis of cell-cell communication using CellChat. Nature Communications 2021 12:1. 2021;12(1):1-20.

50. Kim MC, Gate R, Lee DS, et al. Method of moments framework for differential expression analysis of single-cell RNA sequencing data. Cell. 2024;187(22):6393-6410.e6316.

APPENDICES-1. Supplementary figures

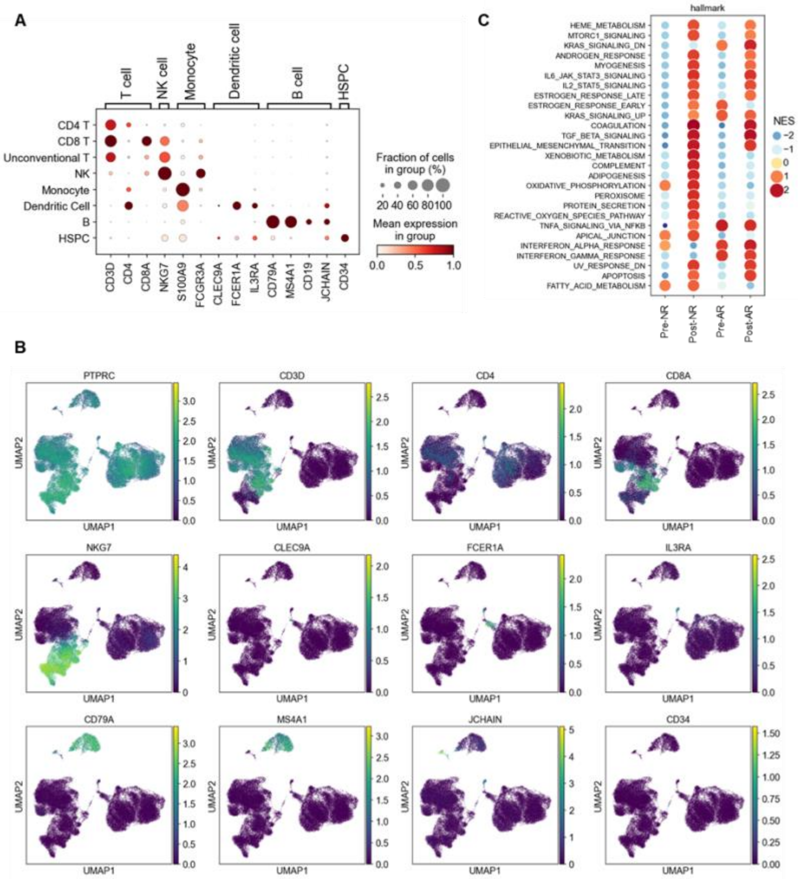

Figure S1. Comprehensive single-cell profiling in liver transplant recipients.

(A) Dotplot showing normalized expression of major immune cell type marker in PBMCs. (B) UMAP plot colored by canonical marker gene expression. (C) GSEA top enriched pathways for each group.

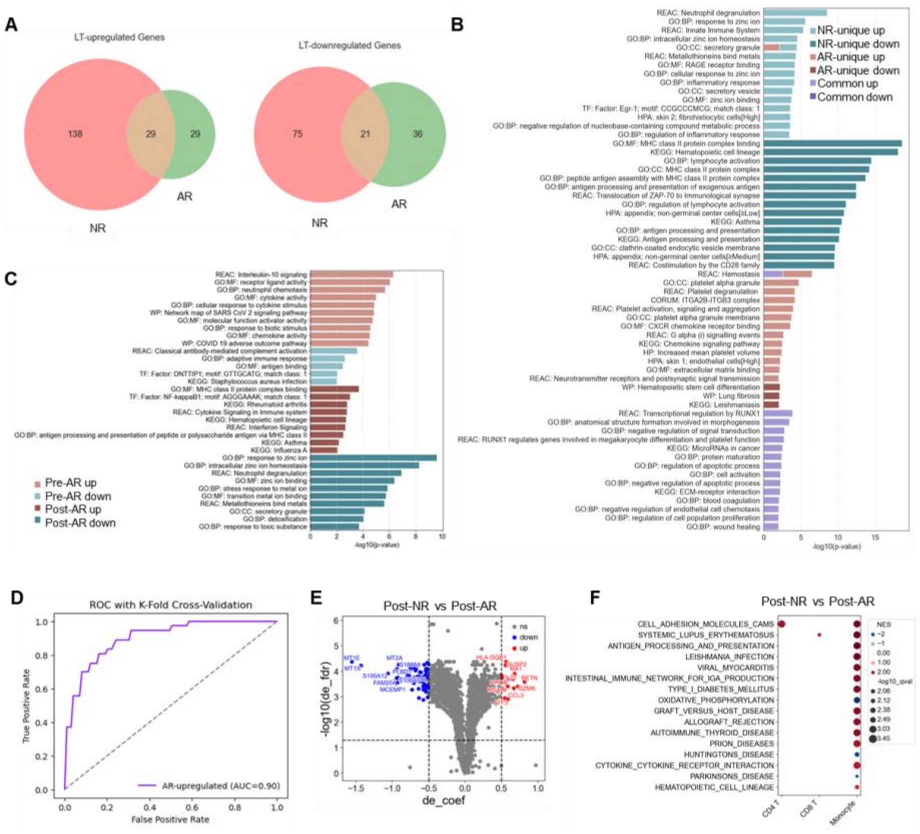

Figure S2. Pre-operative transcriptional signatures of acute rejection.

(A) Venn diagram showing pre- to post-transplantation upregulated (left) or downregulated (right) genes in NR or AR groups. **(B)** Top enriched pathways detected by gProfiler for genes in each compartment of the Venn diagram shown in (A). **(C)** Top enriched pathways detected by gProfiler for DEGs of each group. **(D)** ROC curve for rejection decision model using liver biopsy bulk RNA data (GSE145780). **(E)** Volcano plot displaying differential gene expression in Post-AR compared to Post-NR (de_coeff > 0.5, FDR-corrected p-value < 0.05). **(F)** Dot plot showing enriched molecular pathways in Post-AR samples across different cell types.

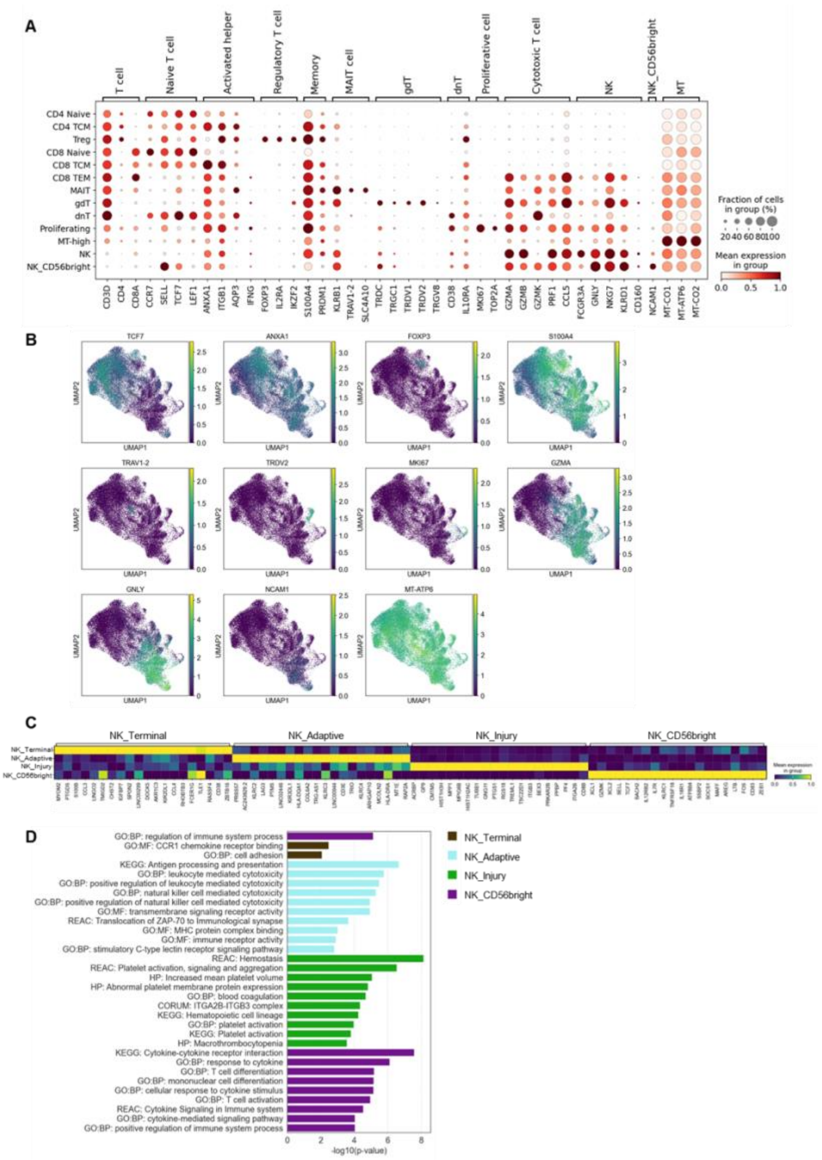

Figure S3. Pre-operative T and NK cell modulation in acute rejection.

(A) Dot plot showing T and NK subtype marker gene expression. **(B)** UMAP plot colored by canonical marker gene expression. **(C)** Heatmap showing normalized expression of NK subpopulation marker genes detected by DEG analysis. **(D)** Top pathways of each NK subpopulation detected by gProfiler using the marker genes.

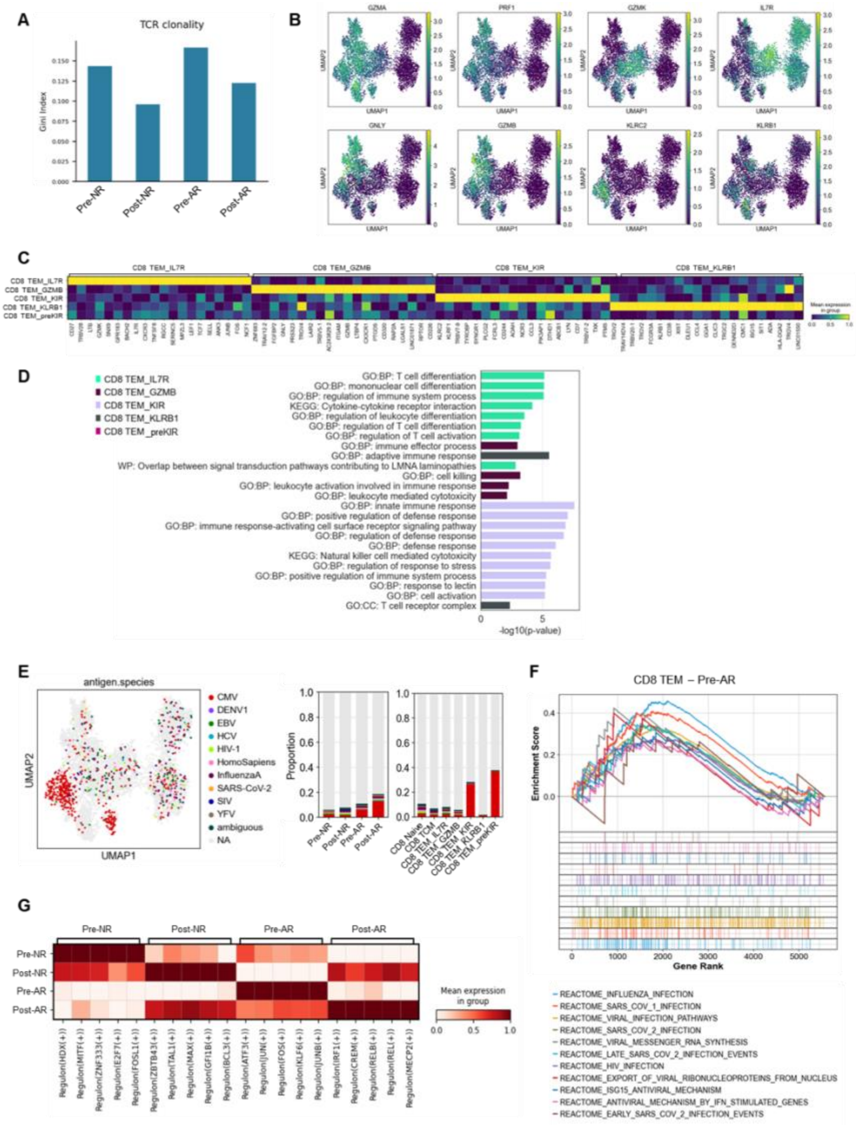

Figure S4. Clonal dynamics and phenotypic transitions of CD8 T cells in acute rejection. (A) TCR clonality indicated by Gini index by group. (B) Effector memory CD8 T cell subpopulation marker gene expression shown in UMAP. (C) Heatmap showing normalized expression of effector memory CD8 T cell subpopulation marker genes detected by DEG analysis. (D) Top pathways of each effector memory CD8 T cell subpopulation detected by gProfiler using the marker genes. (E) UMAP (left) showing the predicted epitope for each CD8 T cell and stacked bar plot (right) showing predicted epitope proportion by group and CD8 T cell subpopulation. (F) NES plot for virus-related pathways enriched in effector memory T cells in Pre-AR group. (G) Heatmap showing relative activities of top regulons of each group.

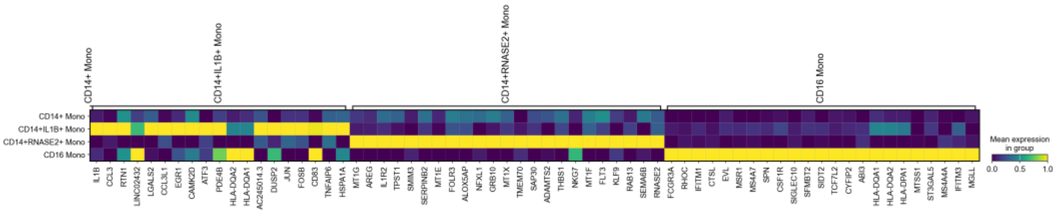

Figure S5. Transcriptomic divergence of monocytes in acute rejection. Heatmap showing normalized expression of monocyte subpopulation marker genes detected by DEG analysis.

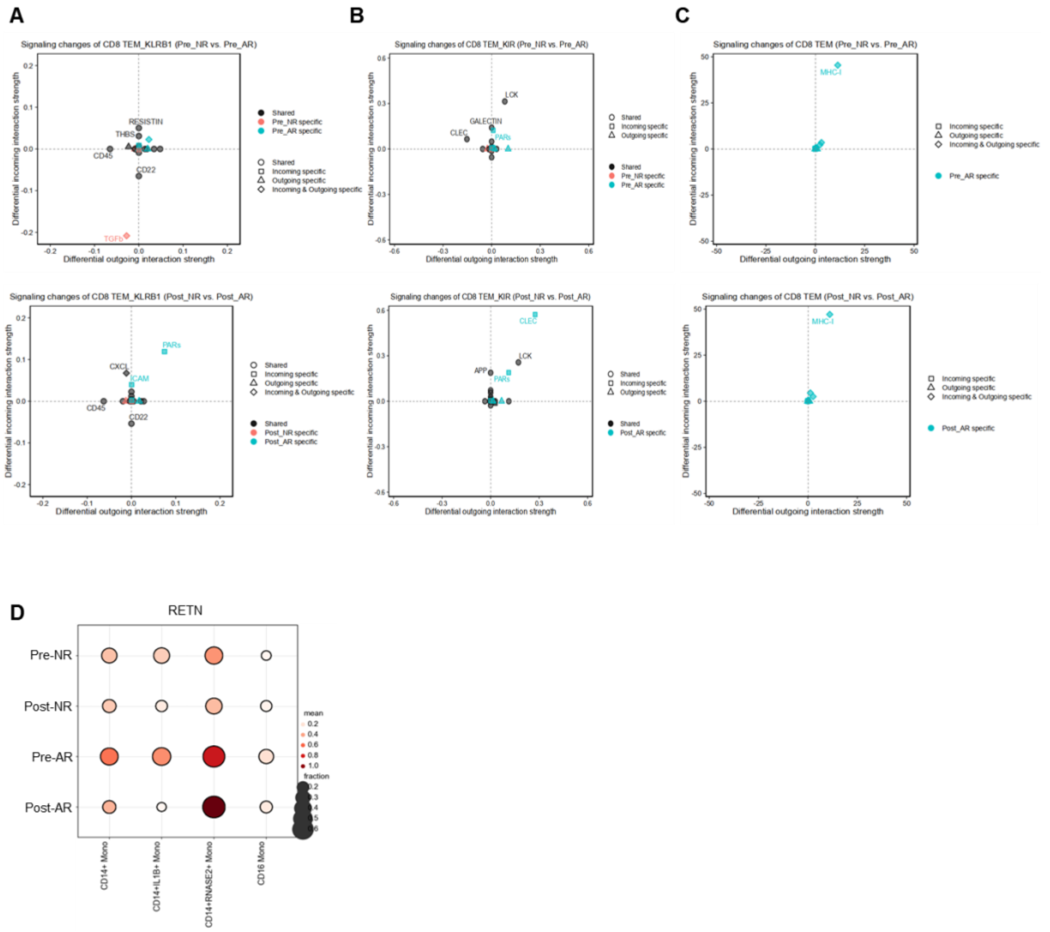

Figure S6. Differences in intercellular dynamics in acute rejection.

(A-C) Differentially activated interactions in Pre-NR versus Pre-AR (top) or Post-NR versus Post-AR (bottom) for CD8 TEM_KLRB1 (left), CD8 TEM_KIR (middle), and CD8 TEM_preKIR (right). (**D**) Mean RETN expression by group and monocyte subpopulations.

APPENDICES-2. Supplementary

Label	Age	Sex	BMI	Hypertension	Diabetes_mellitus	Cardiovascular_disease	Autoimmune	HCC	Pretransplant_MELD	Retransplantation	Combined_transplantation	ABO_incompatibility	LCM	Donor_relation	Donor_age	Donor_sex	OP_time	Transfusion_RBC	Transfusion_FFP	Transfusion_PLT	death_or_gfail	death_or_gfail_surv	rejection_total_new	rejection_total_surv_new
NR_1	70	1	24.913	2	2	1	1	1	13	1	1	2	1	1	40	1	576	4	2	0	0	193	0	193
NR_2	57	1	23.875	1	1	1	1	1	7	1	1	1	1	1	24	1	522	2	0	0	0	578	0	578
NR_3	65	1	18.424	1	1	1	1	1	22	1	1	2	1	1	39	1	384	11	2	6	0	543	0	543
NR_4	67	2	26.164	1	2	2	1	1	14	1	1	1	1	1	46	1	525	2	0	0	0	423	0	423
NR_5	58	2	21.727	1	1	1	1	1	21	1	1	1	1	1	28	1	495	12	5	12	0	568	0	568
NR_6	48	1	37.024	2	1	1	1	2	8	1	1	2	1	1	44	2	540	0	0	0	0	438	0	438
AR_1	71	1	22.806	1	2	1	1	1	11	1	1	2	1	1	39	1	342	2	0	0	0	424	1	9
AR_2	55	1	25.991	1	1	1	1	1	25	1	1	1	1	1	26	2	831	3	4	0	1	60	1	20
AR_3	45	2	15.615	1	1	1	1	1	16	1	1	1	1	2	46	1	384	4	0	0	1	155	1	9
AR_4	55	2	23.066	1	1	1	1	1	29	1	1	1	2	1	28	2	438	7	0	0	0	284	1	14
AR_5	58	1	27.990	2	1	1	1	2	20	1	1	1	1	1	23	1	549	5	3	0	0	189	1	7
AR_6	52	1	22.173	2	1	2	1	1	21	1	1	1	1	1	18	2	693	18	3	6	0	474	1	7

Label	bpr	bpr_surv	pod	Donor_type	psvalue	ast_preLT	ast_w1	ast_w2	alt_preLT	alt_w1	alt_w2	inr_preLT	inr_w1	inr_w2	tbil_preLT	tbil_w1	tbil_w2	taclevel_w1	taclevel_w2	mmf_pod7	mmf_pod14	Underlying liver disease
NR_1	0	193	7	Living	0.245	26	49	55	19	102	108	1.14	1.01	0.97	1.4	1.8	1	6.5	2.5	500	500	Others
NR_2	0	578	14	Living	0.018	51	35	24	19	126	34	1.13	1.21	1.03	1	27.7	1.7	5.7	5.6	NA	NA	HBV
NR_3	0	543	7	Living	0.007	27	60	28	17	74	34	1.48	1.36	1.12	1.7	0.8	1	3.1	1.8	250	250	Alcoholic
NR_4	0	423	14	Living	0.125	27	48	25	19	197	51	1.25	1.07	1.29	2.1	12.8	1.2	2.2	2.4	500	500	Others
NR_5	0	568	7	Living	0.001	71	21	33	62	81	53	2.31	1.14	1.06	6	3.3	1.3	4.5	5.8	NA	NA	HBV
NR_6	0	438	7	Living	0.078	36	20	20	15	44	8	1.42	1.2	1.16	1.2	1.4	0.8	3.5	3.2	250	250	HBV
AR_1	1	9	7	Living	0.238	31	106	32	5	159	16	1.31	0.99	1.1	2.4	11.3	2.4	11	2.5	500	250	Alcoholic
AR_2	1	20	14	Living	0.095	27	35	41	14	92	31	1.25	1.05	NA	2.2	1.5	1.3	4.4	4.5	NA	NA	Alcoholic
AR_3	0	155	7	Living	NA	20	25	44	5	27	11	1.25	1.5	1.37	0.9	5.6	2.5	6	5.3	NA	500	Alcoholic
AR_4	0	284	14	Living	NA	30	344	101	13	318	40	1.22	1.1	0.9	3.4	8.5	2.6	2	3	NA	NA	Others
AR_5	0	189	7	Living	NA	38	37	62	10	81	358	1.33	1.09	1.06	3.6	1.5	0.9	4.2	5	NA	NA	HBV
AR_6	0	474	7	Living	NA	20	27	28	18	26	36	1.07	1.13	1.22	0.6	2	2.6	8.6	5.3	NA	NA	Others

1=False, 2=True; 1=M, 2=F (for sex); BMI, body mass index; HCC, hepatocellular carcinoma; MELD, model for end-stage liver disease; LCM, lymphocyte cross-matching; OP, operation; RBC, red blood celll; FFP, fresh frozen plasma; PLT, platelet; gfail, graft-failure; ast, aspartate aminotransferase; alt, alanine aminotransferase; inr, international normalized ratio; tbil, total bilirubin; tac, tacrolimus; mmf, mycophenolate mofetil; pod, post operative day

Table S1. Clinical metadata of samples

Abstract in Korean

단일세포 RNA 시퀀싱 기반 말초혈액단핵세포 분석을 통한 간이식 후 급성 거부 반응 예측

간이식은 말기 간질환에 대한 궁극적인 치료법임. 그러나 전체 수혜자의 약 15–30%에서 급성 이식편 거부반응이 발생함. 현재까지 조기 예측은 제한적이며, 진단은 여전히 침습적인 조직생검에 의존하고 있음. 본 연구에서는 간이식 수혜자의 수술 전후 말초혈액 단핵세포(peripheral blood mononuclear cells, PBMCs)를 대상으로 단일세포 RNA 시퀀싱(single-cell RNA sequencing) 및 T세포 수용체(T cell receptor, TCR) 레퍼토리 분석을 수행하였으며, 급성 거부반응(acute rejection, AR)과 연관된 분자적 특징을 규명하였음.

거부반응이 발생한 환자들은 수술 전부터 특이적인 면역 상태를 보였으며, 염증성 자연살해세포(NK cells), 클론 확장된 effector memory CD8 T 세포, 변화된 단핵구 아형이 특징적으로 관찰되었음. 이식 후 이러한 면역세포들은 지속적인 염증 반응을 나타내었으며, 면역억제 치료 하에서도 바이러스 특이적 CD8 T 세포가 풍부하게 나타나는 등 거부반응 특이적 재프로그래밍이 일어났음.

CCL3, GZMK, MX1, RETN, ATF3 등 다섯 개 유전자는 수술 전후 급성거부반응 환자 샘플에서 지속적으로 상향 조절되었음. 이 중 CCL3, GZMK, MX1은 대규모 공개 간 조직 생검 데이터셋에서도 상향 조절되어있는것이 검증되었으며, 각각 백혈구 유주, 세포독성, 항바이러스 반응과 관련된 역할을 수행함. RETN과 ATF3는 거부반응 연관 단핵구에서 각각 분비성 리간드 및 활성화 전사인자로 기능적으로 특징지어졌음. 이러한 유전자를 이용한 급성 거부반응의 예측모델은 우수한 예측 성능(AUC = 0.90)을 보였음.

본 연구결과는 간이식 후 거부반응의 비침습적 위험도 평가 및 조기 진단의 기반이 될 수 있음. 또한, 개인 맞춤형 면역조절 치료 전략 개발을 위한 단서도 제시함.

핵심되는 말 : 간이식, 급성 거부반응, 단일세포 RNA 시퀀싱, 말초혈액 단핵세포